

Depth Estimation From Monocular Images With Enhanced Encoder-Decoder Architecture

Dabbrata Das , Argho Deb Das  and Farhan Sadaf ^{*}

Department of Computer Science and Engineering, Khulna University of Engineering & Technology, Khulna - 9203, Bangladesh.

ARTICLE INFO

Keywords:

Monocular Depth Estimation
Depth Map
Encoder-Decoder Architecture
Inception-ResNet-v2 (IRv2)
NYU Depth V2
Computer Vision

ABSTRACT

Estimating depth from a single 2D image is a challenging task because of the need for stereo or multi-view data, which normally provides depth information. This paper deals with this challenge by introducing a novel deep learning-based approach using an encoder-decoder architecture, where the Inception-ResNet-v2 model is utilized as the encoder. According to the available literature, this is the first instance of using Inception-ResNet-v2 as an encoder for monocular depth estimation, illustrating better performance than previous models. The use of Inception-ResNet-v2 enables our model to capture complex objects and fine-grained details effectively that are generally difficult to predict. Besides, our model incorporates multi-scale feature extraction to enhance depth prediction accuracy across different kinds of object sizes and distances. We propose a composite loss function consisting of depth loss, gradient edge loss, and SSIM loss, where the weights are fine-tuned to optimize the weighted sum, ensuring better balance across different aspects of depth estimation. Experimental results on the NYU Depth V2 dataset show that our model achieves state-of-the-art performance, with an ARE of 0.064, RMSE of 0.228, and accuracy ($\delta < 1.25$) of 89.3%. These metrics demonstrate that our model effectively predicts depth, even in challenging circumstances, providing a scalable solution for real-world applications in robotics, 3D reconstruction, and augmented reality.

1. Introduction

Scene depth estimation is a crucial task in computer vision that significantly enhances machine perception and comprehension of three-dimensional (3D) environments. Depth estimate is crucial for various applications, including autonomous driving, robotic navigation, virtual reality (VR), and augmented reality (AR). In these fields, precise depth information helps machines to efficiently interact with the actual world, ensuring safe navigation, accurate object detection, and realistic interaction with virtual environments.

Traditional depth estimation techniques, such as stereo vision and active depth sensing using LiDAR [1] or structured light, have been widely used to generate depth maps. These methods are effective but often require specialized hardware setups, including multiple cameras or expensive depth sensors, which significantly increase the cost and complexity of the system. For example, in autonomous driving, LiDAR systems provide highly accurate depth maps, but their high cost and resource requirements limit their broad deployment. This has increased demand for more scalable and cost-effective solutions, particularly in scenarios where only a single camera is available.

Monocular depth estimation, which derives depth from a singular 2D image, has emerged as an appealing alternative due to its simplicity and minimal technology prerequisites. It removes the need for stereo vision systems or depth sensors, making it compatible with various devices, including mobile phones and drones. This challenge is tricky because, without stereo information, accurately estimating depth from a single image becomes more difficult. Problems like telling

apart objects of different sizes or figuring out if one object is blocking another make monocular depth estimation especially difficult.

Early studies on monocular depth estimation predominantly utilized hand-crafted features and geometric indicators such as vanishing points, shadows, and defocus. These methods worked well in simple environments but struggled in complex real-world scenes. With machine learning, models using techniques like Scale-Invariant Feature Transform (SIFT) [2] and Conditional Random Fields (CRF) [3] improved depth map predictions by learning from data. However, these models still had trouble working well in different types of scenes because they relied too much on hand-made features.

The recent growth of deep learning has significantly improved monocular depth estimation. Convolutional Neural Networks (CNNs), which can learn complex patterns directly from raw image data, are replacing traditional handcrafted features. Models proposed by Kim et al. [4] and Laina et al. [5] demonstrate that deep neural networks can accurately predict dense, high-resolution depth maps with significant accuracy, even in challenging environments. Moreover, the integration of Generative Adversarial Networks (GANs) [6] and attention mechanisms has advanced the field even further. Schlett et al. [7] addresses the challenge of 3D multi-person pose estimation by proposing a pipeline for absolute 3D human pose recovery. It introduces a dual-branch structure for human root localization and uses attention mechanisms to enhance the accuracy of relative and absolute pose estimation. Qiao et al. [8] introduce an innovative multi-stage depth super-resolution network that utilizes explicit high-frequency data from a transformer and implicit signals from the frequency domain to improve depth map reconstruction.

This paper focuses on advancing monocular depth esti-

^{*}Corresponding author

¹Data: <https://www.kaggle.com/datasets/soumikrakshit/nyu-depth-v2>

²GitHub: <https://github.com/dabbrata/Depth-Estimation-Enc-Dec>

Nomenclature

<i>ARE</i>	Absolute Relative Error	<i>MARE</i>	Mean Absolute Relative Error
<i>CNN</i>	Convolutional Neural Network	<i>MSE</i>	Mean Square Error
<i>DNN</i>	Deep Neural Network	<i>R - A</i>	Reduction A
<i>GANVO</i>	Generative Adversarial Network for Visual Odometry	<i>R - B</i>	Reduction B
<i>GNN</i>	Generative Adversarial Network	<i>R²</i>	Coefficient of Determination
<i>IR - A</i>	Inception Resnet A	<i>RELU</i>	Rectified Linear Unit
<i>IR - B</i>	Inception Resnet B	<i>RESNET</i>	Residual Network
<i>IR - C</i>	Inception Resnet C	<i>RMSE</i>	Root Mean Square Error
<i>IRv2</i>	Inception Resnet V2	<i>RNN</i>	Recurrent Neural Network
<i>LOG10</i>	Logarithmic Base 10	<i>SGANVO</i>	Stacked Generative Adversarial Network for Visual Odometry
<i>LR</i>	Linear Regression	<i>SSIM</i>	Structural Similarity Index Measure
<i>LSTM</i>	Long Short-Term Memory		

mation using deep learning, proposing a novel architecture based on Inception-ResNet-v2[9], which succeeds at capturing multi-scale features and refining depth predictions. Our contributions include a customized loss function which includes depth loss, gradient edge loss, and SSIM loss to optimize both the accuracy and structural consistency of depth maps. We illustrate the efficacy of our methodology through experiments on the NYU Depth V2 dataset [10], where our model surpasses leading encoder-decoder based techniques in accuracy.

The remaining parts of this work are structured as follows: Section II examines pertinent literature in monocular depth estimation, emphasizing significant progress in deep learning. Section III presents the approach and model's architecture, while Section IV covers the dataset, training procedure, and specifics of implementation. Section V includes the results and analysis, while Section VI finishes with future prospects and problems in the field.

2. Related Works

Related literature encompasses a diverse array of supervised deep learning techniques extensively researched and implemented in monocular depth estimation, mostly comprising CNN-based, RNN-based, and GAN-based models.

2.1. RNN-based methods

Kumar et al. [11] introduced an innovative convolutional LSTM-based [12] recurrent neural network architecture for monocular depth estimation from video sequences. Their methodology intended to take advantage of temporal dependencies between video frames, and they evaluate it using the KITTI dataset[13]. The best-performing model achieved an absolute relative error of 0.137. Mancini et al. [14] improved scene depth prediction by adding LSTM[12] units after the encoder network's convolutional layers. Their approach, as evaluated on the KITTI dataset[13], significantly

improved generalization, achieving an RMSE(log) of 0.366 and an Absolute Relative Difference of 0.312.

2.2. GAN-based methods

Jung et al. [15] introduced Generative Adversarial Networks (GANs) for monocular depth estimation, employing a GlobalNet to extract global features and a RefinementNet to ascertain local structures from a single image, utilizing the NYU v2 [10] dataset. Their method achieved significant improvement, with an ARE of 0.134. Lore et al. [16] introduced a depth map estimation technique utilizing Conditional Generative Adversarial Networks (cGANs). The methodology was assessed using the NYU Depth v2 dataset [10], resulting in a root mean square error (RMSE) of 0.875. Their model outperformed traditional non-parametric sampling methods. Feng and Gu [17] devised an unsupervised methodology for depth and ego-motion estimation with Stacked GANs (SGANVO). The model surpassed current techniques in depth estimation on the KITTI dataset [13], with an average RMSE log of 0.1623 across a number of scenarios. Aleotti et al. [18] developed an unsupervised monocular depth prediction model based on GANs. The model outperformed previous approaches on the KITTI [13] and Cityscapes [19] datasets, with an RMSE log of 0.185 and ARE of 0.102. It improved depth prediction accuracy and produced more realistic image warps. Li et al. [20] introduced a depth estimation technique utilizing Conditional GAN, integrating monocular RGB pictures with sparse point clouds. Their methodology utilized the NYU-Depth-v2 dataset [10], achieving a root mean square error (RMSE) of 0.256 and a mean absolute relative error (MARE) of 0.046, surpassing prior techniques. Almalioglu et al. [21] proposed an unsupervised deep learning framework using GAN for monocular visual odometry and depth estimation. They evaluated their methodology on KITTI [13] and Cityscapes datasets [19] and achieved superior performance with RMSE of 5.448 and RMSE(log) of 0.216. Widya et al. [22] established a self-supervised monocular depth estimation framework utilizing GAN-enhanced pictures. They

Table 1
Summary of Impactful Works in Depth Estimation of Deep Learning

Reference	Analysis Type	Model	Technique	Dataset	Performance
Kumar et al. [11]	RNN-based	Convolutional LSTM	Utilized temporal dependencies between video frames	KITTI	Absolute Relative Error: 0.137
Mancini et al. [14]	RNN-based	LSTM-enhanced CNN	Added LSTM units after encoder's convolutional layers	KITTI	RMSE(log): 0.366, ARE: 0.312
Shi et al. [24]	RNN-based	Convolutional LSTM	Improved over ROVER algorithm	Radar Echo Dataset	Rainfall-MSE: 1.420
Jung et al. [15]	GAN-based	GlobalNet + RefinementNet	Extracted global features and estimated local structures	NYU Depth v2	ARE: 0.134
Lore et al. [16]	GAN-based	Conditional GANs	Improved depth map estimation with cGANs	NYU Depth v2	RMSE: 0.875
Li et al. [25]	CNN-based	VGG-16-based System	Fused depth and depth gradients	NYU Depth v2	RMSE: 0.611
Lee and Kim [26]	CNN-based	Encoder-Decoder CNN	Combined depth maps at multiple scales	NYUv2 and KITTI	RMSE(log): 0.180 on NYUv2
Xu et al. [27]	CNN-based	Structured Attention Model	Integrated multi-scale characteristics and attention mechanisms	NYU Depth V2 and KITTI	ARE: 0.125 on NYUv2

trained their model on the gastroendoscopic dataset [23] and gained an RMSE of 1.2232 and a relative error of 0.2005, showing increased accuracy in both chromoendoscopic and general endoscopic images.

2.3. CNN-based methods

Zoran et al. [28] established a deep learning framework for mid-level vision tasks that acquires ordinal correlations among picture points. Utilizing the NYU Depth v2 [10] dataset, their model achieved an RMSE(log) of 0.42 in depth estimation. Li et al. [25] introduced a dual-stream system utilizing VGG-16 [29] for depth estimation from individual RGB pictures, employing the NYU Depth v2 [10] dataset. Their model integrated depth and depth gradients to enhance local detail and depth precision, achieving an RMSE of 0.611. Chen et al. [30] introduced a deep neural network for single-image depth estimation utilizing the Depth in the Wild (DIW) dataset. Their approach, integrating relative depth annotations with metric depth, attained an RMSE of 1.13, surpassing previous methods on real-world, everyday photos. Lee and Kim [26] created a convolutional neural network using an encoder-decoder architecture for depth estimation utilizing the NYUv2 [10] dataset. Their approach achieved an RMSE(log) of 0.180, improving accuracy by effectively combining depth maps at multiple scales. Xu et al. [27] formulated a structured attention-guided conditional neural field model for the estimation of monocular depth. The integration of multi-scale characteristics and attention mechanisms resulted in superior performance compared to previous CRF-based models, achieving an ARE of 0.125 on

the NYU Depth V2 dataset [10] and 0.122 on the KITTI dataset [13]. Kim et al. [4] introduced a deep variational model for monocular depth estimation, integrating global and local predictions from two CNNs. Their model achieved an RMSE(log) of 0.172 on the NYU v2 [10] dataset. Zhang et al. [31] introduced an innovative, progressive hard-mining network (PHN) for monocular depth estimation. Their approach utilized multi-scale refinement and hard-mining loss, attaining an ARE of 0.512 and 0.179 on the NYU Depth V2 [10] and Make3D datasets [32], respectively. Laina et al. [5] created a fully convolutional residual network for monocular depth estimation, incorporating an innovative up-sampling method to enhance output resolution. Their model attained an Average Relative Error (ARE) of 0.127 on the NYU Depth V2 dataset [10] and 0.176 on the Make3D dataset [32] respectively.

3. Methodology

This section provides a comprehensive explanation of data preprocessing and model architecture with detailed workflow and loss functions.

3.1. Preprocessing

Preprocessing the images is a crucial step in building the model, as it ensures better results before passing the data into it. We first applied the min-max normalization equation (1), a linear transformation that scales the image intensity values

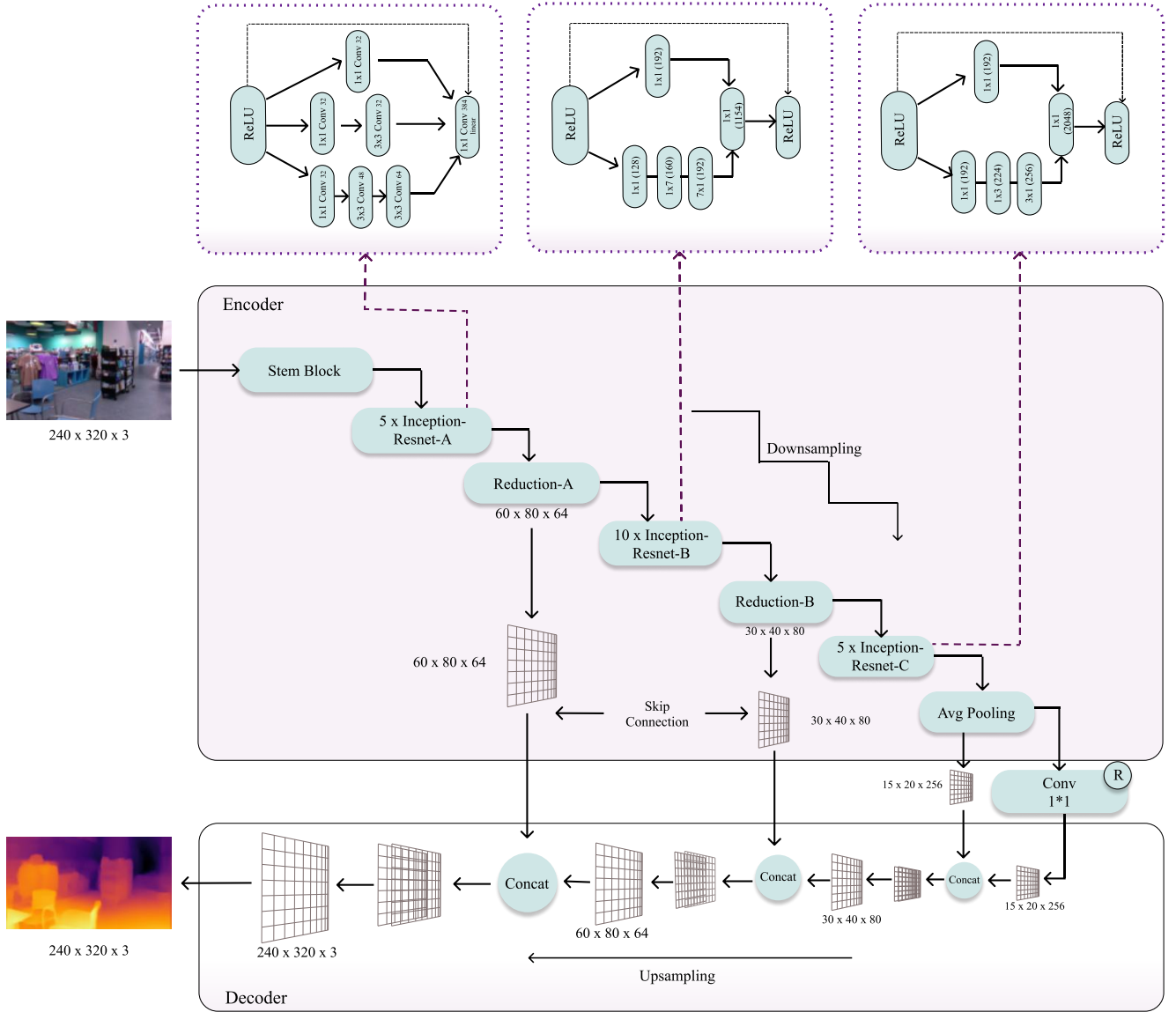


Figure 1: An outline of our network (encoder-decoder) architecture. The encoder uses a pre-trained Inception-ResNet V2 (IRv2) [9] network, consisting of several Inception-ResNet blocks (A, B, and C) and reduction layers. The decoder consists of convolutional layers that process the upsampled output from the previous layer, combined with the corresponding feature maps from the encoder.

between 0 and 1.

$$\bar{x} = \frac{x - x_{\min}}{x_{\max} - x_{\min}} \quad (1)$$

Here, the normalized value is \bar{x} , and the original value is x . Data augmentation, including horizontal flipping of images, is also applied during the preprocessing steps.

3.2. Network Architecture

Our model makes use of an encoder-decoder architecture based on deep convolutional neural networks, implemented using the TensorFlow [33]. The decoder network employs deconvolution layers to produce the depth map by pixel-by-pixel estimation that matches the input size, while the encoder network utilizes convolution and pooling layers

to acquire depth data. In the encoding and decoding stages, downsampling and upsampling are performed, respectively.

3.2.1. Encoder

In the encoder section, we used the Inception-ResNet-v2 (IRv2)[9] architecture as a pre-trained model. Downsampling is performed through the truncated layers of this pre-trained model. By passing the images through these layers, we will extract more accurate features from the images. In Inception-Resnet-v2 architecture, three categories of inception blocks exist (Inception Resnet Block A, Inception Resnet Block B, Inception Resnet Block C), two types of reduction blocks (Reduction Block A and B), as well as a Stem Block and an Average Pooling layer. The inception blocks

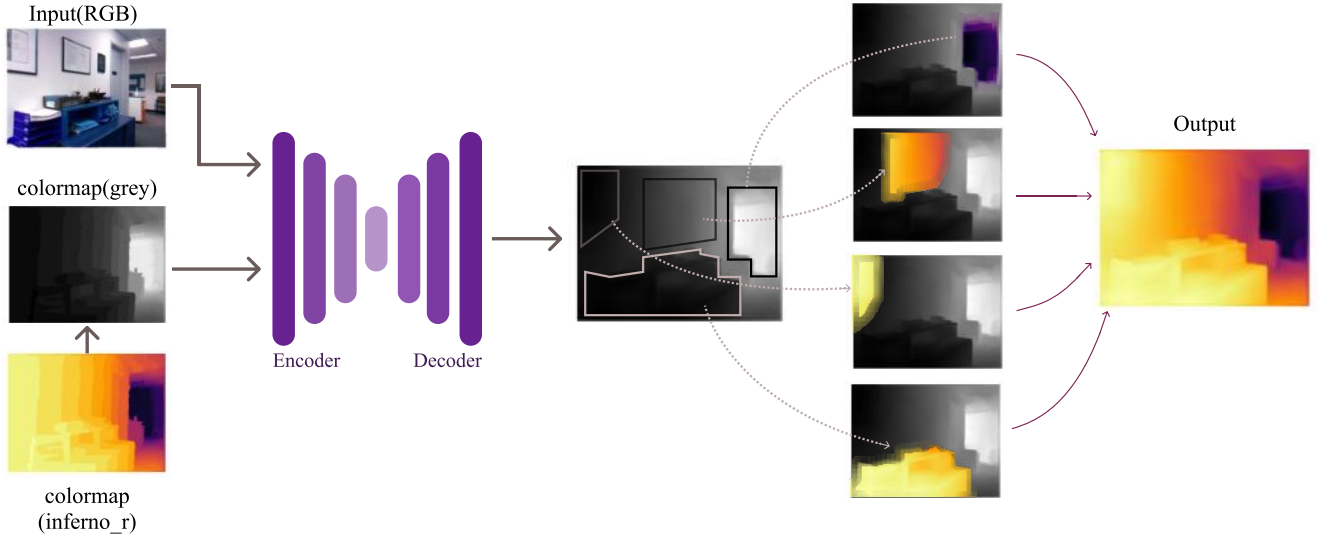


Figure 2: Process of generating a color map by mapping depth information from a grayscale image using an encoder-decoder network.

are repeated multiple times to form the full-layer architecture.

IR-A. The Inception-ResNet-A block is a crucial component of the Inception-ResNet-v2 architecture. It is designed to capture multi-scale features and reduce the vanishing gradient problem. This block typically comprises multiple parallel branches, each utilizing different convolutional kernel sizes, including Conv(1x1), Conv(3x3), and Conv(5x5). Residual connections within the block facilitate improved gradient flow during both forward and backward passes, addressing the vanishing gradient issue and enhancing the training of deep networks. The activation functions, typically ReLUs, are applied after each convolution to stabilize and activate the features. The structure of the Inception-ResNet-A block is represented in Algorithm 1:

Algorithm 1: Inception-ResNet Block A (IR_A)

Input : Feature map x

Output: Processed feature map $IR_A(x)$

```

1  $z_1 \leftarrow \text{Conv}(x, 1 \times 1)$ ;
2  $z_2 \leftarrow \text{Conv}(z_1, 3 \times 3)$ ;
3  $z_3 \leftarrow \text{Conv}(z_2, 3 \times 3)$ ;
4  $z_{\text{concat}} \leftarrow \text{Concat}(z_1, z_2, z_3)$ ;
5  $z_4 \leftarrow \text{Conv}(z_{\text{concat}}, 1 \times 1)$ ;
6  $IR_A(x) \leftarrow \text{ReLU}(x + z_4)$ ;
7 return  $IR_A(x)$ ;
    
```

R-A. The Reduction-A block reduces spatial dimensions and parameters using convolutional layers with strides greater than 1 or pooling operations. It is crucial for compressing feature maps while retaining essential information, improving computational efficiency, and generating more compact feature representations. The simplified algorithm of the block is outlined in Algorithm 2.

IR-B. Inception-Resnet-B is another convolution block

Algorithm 2: Reduction Block A (R_A)

Input : Feature map x

Output: Processed feature map $R_A(x)$

```

1  $x \leftarrow IR_A(x)$ ;
2  $z_1 \leftarrow \text{MaxPool}(x, 3 \times 3, s = 2)$ ;
3  $z_2 \leftarrow \text{Conv}(x, 3 \times 3, s = 2)$ ;
4  $z_3 \leftarrow \text{Conv}(x, 1 \times 1)$ ;
5  $z_4 \leftarrow \text{Conv}(z_3, 3 \times 3)$ ;
6  $z_5 \leftarrow \text{Conv}(z_4, 3 \times 3, s = 2)$ ;
7  $R_A(x) \leftarrow \text{Concat}(z_1, z_2, z_5)$ ;
8 return  $R_A(x)$ ;
    
```

consisting of a 7×7 convolution filter where the filter is factorized into 1×7 and 7×1 , two asymmetric convolutions. By factorizing, the quantity of parameters is decreased, while the 1×1 convolution applied before the 7×7 convolution further limits the parameter count and enhances computational efficiency. The simplified representation of the block is described in Algorithm 3.

Algorithm 3: Inception-ResNet Block B (IR_B)

Input : Feature map x

Output: Processed feature map $IR_B(x)$

```

1  $x \leftarrow R_A(x)$ ;
2  $z_1 \leftarrow \text{Conv}(x, 1 \times 7)$ ;
3  $z_2 \leftarrow \text{Conv}(x, 7 \times 1)$ ;
4  $z_{\text{concat}} \leftarrow \text{Concat}(z_1, z_2)$ ;
5  $z_3 \leftarrow \text{Conv}(z_{\text{concat}}, 1 \times 1)$ ;
6  $IR_B(x) \leftarrow \text{ReLU}(x + z_3)$ ;
7 return  $IR_B(x)$ ;
    
```

R-B. The Reduction-B block reduces spatial dimensions while increasing channel depth, helping the Inception-ResNet-v2 model capture high-level features efficiently during down-sampling. The simplified algorithm of the block is repre-

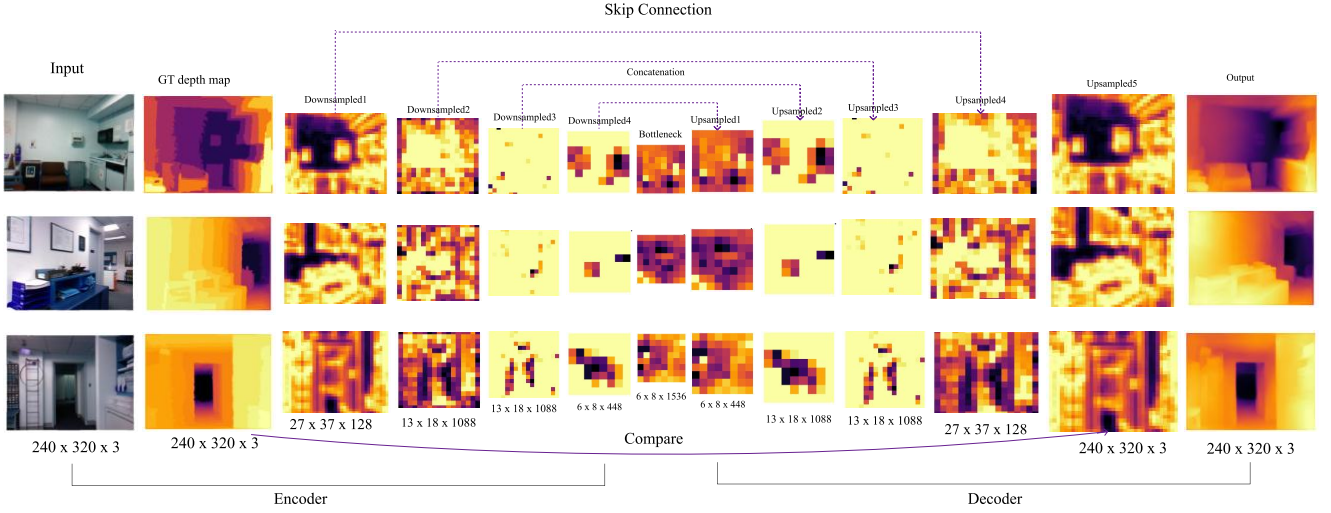


Figure 3: Feature map representation within the encoder-decoder network architecture utilized for depth map generation.

sented by Algorithm 4.

Algorithm 4: Residual Block B (R_B)

Input : Feature map x

Output: Processed feature map $R_B(x)$

```

1  $x \leftarrow IR_B(x)$ ;
2  $z_1 \leftarrow \text{MaxPool}(x, 3 \times 3, s = 2)$ ;
3  $z_2 \leftarrow \text{Conv}(x, 1 \times 1)$ ;
4  $z_3 \leftarrow \text{Conv}(z_2, 3 \times 3, s = 2)$ ;
5  $z_4 \leftarrow \text{Conv}(x, 1 \times 1)$ ;
6  $z_5 \leftarrow \text{Conv}(z_4, 3 \times 3)$ ;
7  $z_6 \leftarrow \text{Conv}(z_5, 3 \times 3, s = 2)$ ;
8  $R_B(x) \leftarrow \text{Concat}(z_1, z_3, z_6)$ ;
9 return  $R_B(x)$ ;
    
```

IR-C. Inception-Resnet-C is another inception block in Inception-Resnet-v2 architecture where a 3×3 convolution filter is used, and before it, 1×1 convolution is also used to reduce the parameters. Here, 3×3 convolution is also factorized into two asymmetric convolutions. The convolutions occur parallelly, and finally, all the outputs are concatenated. This allows the network to focus on capturing more abstract and higher-level data from the image. Here, Algorithm 5 represents the simplified representation of the block.

Algorithm 5: Inception-ResNet Block C (IR_C)

Input : Feature map x

Output: Processed feature map $IR_C(x)$

```

1  $x \leftarrow R_B(x)$ ;
2  $z_1 \leftarrow \text{Conv}(x, 1 \times 3)$ ;
3  $z_2 \leftarrow \text{Conv}(x, 3 \times 1)$ ;
4  $z_{\text{concat}} \leftarrow \text{Concat}(z_1, z_2)$ ;
5  $z_3 \leftarrow \text{Conv}(z_{\text{concat}}, 1 \times 1)$ ;
6  $IR_C(x) \leftarrow \text{ReLU}(x + z_3)$ ;
7 return  $IR_C(x)$ ;
    
```

Algorithm 6: Inception-ResNet-v2 ($IRv2$) Encoder with Repeated Blocks

Input : Feature map x

Output: Encoded feature map $IRv2_Encoder(x)$

```

1 Repeat  $IR\_A$  block 10 times:
2  $i \leftarrow 1$ ;
3 while  $i \leq 10$  do
4    $x \leftarrow IR\_A(x)$ ; [Algorithm 1]
5    $i \leftarrow i + 1$ ;
6 end
7 Apply  $R\_A$  block:
8  $x \leftarrow R\_A(x)$ ; [Algorithm 2]
9 Repeat  $IR\_B$  block 5 times:
10  $i \leftarrow 1$ ;
11 while  $i \leq 5$  do
12    $x \leftarrow IR\_B(x)$ ; [Algorithm 3]
13    $i \leftarrow i + 1$ ;
14 end
15 Apply  $R\_B$  block:
16  $x \leftarrow R\_B(x)$ ; [Algorithm 4]
17 Repeat  $IR\_C$  block 10 times:
18  $i \leftarrow 1$ ;
19 while  $i \leq 10$  do
20    $x \leftarrow IR\_C(x)$ ; [Algorithm 5]
21    $i \leftarrow i + 1$ ;
22 end
23 return  $x$ ;
    
```

3.2.2. Decoder

After downsampling the image in the encoder section, the resolution will become too low, losing some important features. As the number of features of the images is lower than the original size, it is necessary to reconstruct the image to increase the image's resolution before concatenation. The process of increasing the image size from a lower number of parameters to a higher number of parameters is called up-sampling. This process will be started from the bottleneck

situation of the architecture whether the bottleneck situation means the simplest form of the image with some specific important features. We use the LeakyRelu activation function before starting upsampling from the bottleneck. Here, LeakyRelu is used to avoid neuron inactivity, ensures gradient flow, preserves information, and leads to faster, more stable convergence in this stage. Then upsampling of the image is necessary to concatenate the upsampled image with its corresponding downsampled image through a skip connection Figure 1. A skip connection is a mechanism in neural networks that allows the input from one layer to concatenate straight to a subsequent layer, skipping one or more intermediate layers in the process, helping to preserve important information and reduce vanishing gradient problems. This concatenation is necessary because it helps recover the features that were lost from the image during the earlier stages of processing. Here, skip connections enable the decoder to retrieve high-resolution feature maps from the encoder, guaranteeing the preservation of these features in the final depth map. In the final stage of the model, an activation function (sigmoid) is applied to the depth map output to ensure that the predicted values are appropriately scaled between 0 and 1, providing a normalized representation of the depth information.

3.3. Output

An anticipated depth map is its output, which is generated by our model. After passing an RGB image as input, the trained model will generate a depth map. A depth map represents the distance from a viewpoint to the objects in the scene where the closer objects make it darker and farther objects make it lighter in case of a grayscale image, or vice versa. But for considering the depth map in a color image, the color is in the range of bright yellow to dark purple. All the colors between this color range will be allowed to represent the depth map with respect to the objects of the image. In our model, If an object in the image is closer to the viewpoint than the other objects, then it will be gradually brighter yellow. On the contrary, more distance makes the objects more darker purple. So, we use the Inferno_r color map to represent the depth map as output. The Inferno_r, which is available as an inbuilt color map in Python, is a reversed version of the Inferno, featuring a perceptually uniform gradient that transitions from dark purple to bright yellow, commonly used for visually representing data in heatmaps or scientific visualizations. In the case of color map representation, there are two steps that always happen. Firstly, the model generates a grayscale image as a depth map. This means that each pixel's color is reduced to a single-intensity value. After that, the grayscale values are then mapped to colors in the Inferno_r colormap. As a result, low grayscale values (close to black in grayscale) would be mapped to bright yellow, and high grayscale values (close to white in grayscale) would be mapped to dark purple.

3.4. Loss function

The discrepancy between y , the ground truth depth map, and \hat{y} , the anticipated depth map, is taken into account by a

typical loss function for depth regression issues. The training pace and total depth estimation performance can be greatly impacted by various loss function factors. A wide range of loss function modifications are used to optimize the neural network Neural network for estimating depth. In our method, a composite loss function equation (2) is used, which helps to increase the model's accuracy by tuning the weight. For training the model, loss L is defined between y and \hat{y} as the weighted sum of three loss functions.

$$L(y, \hat{y}) = w_1 L_{\text{depth}}(y, \hat{y}) + w_2 L_{\text{grad}}(y, \hat{y}) + w_3 L_{\text{SSIM}}(y, \hat{y}) \quad (2)$$

Here, w_1 , w_2 , and w_3 are the weights assigned to different losses. L_{depth} , L_{grad} , and L_{SSIM} are depth, gradient, and SSIM loss terms, respectively.

3.4.1. Depth Loss

Here, the loss term L_{depth} refers to point-wise loss, a typical loss function for all techniques based on deep learning. The pixel-by-pixel discrepancy between the anticipated depth map and the actual depth map is estimated by calculating the average of these absolute discrepancies throughout every pixel in the image.

$$L_{\text{depth}}(y, \hat{y}) = \frac{1}{n} \sum_p^n |y_p - \hat{y}_p| \quad (3)$$

3.4.2. Gradient Edge Loss

The term gradient edge loss L_{grad} is measured by calculating the mean absolute disparity between the real depth and the anticipated depth's vertical and horizontal gradients.

$$L_{\text{grad}}(y, \hat{y}) = \frac{1}{n} \sum_p^n |g_x(y_p, \hat{y}_p)| + |g_y(y_p, \hat{y}_p)| \quad (4)$$

Here, g_x and g_y represent horizontal edges and vertical edges, respectively.

3.4.3. Structural Similarity (SSIM) Loss

Finally, the loss term L_{SSIM} is accustomed to determining how well the structural features are retained when comparing the projected depth map to the ground truth depth map. The initial task of calculating the structural loss is to determine the SSIM index.

$$L_{\text{SSIM}}(y, \hat{y}) = \frac{1 - \text{SSIM}(y, \hat{y})}{2} \quad (5)$$

$$\text{SSIM}(y, \hat{y}) = \frac{(2\mu_y\mu_{\hat{y}} + C_1)(2\sigma_{y\hat{y}} + C_2)}{(\mu_y^2 + \mu_{\hat{y}}^2 + C_1)(\sigma_y^2 + \sigma_{\hat{y}}^2 + C_2)} \quad (6)$$

Here, the means of y and \hat{y} are denoted by μ_y and $\mu_{\hat{y}}$, respectively. The variances are σ_y^2 and $\sigma_{\hat{y}}^2$, and the covariance between y and \hat{y} is $\sigma_{y\hat{y}}$. The constants used to stabilize the division are C_1 and C_2 .

Algorithm 7: Training the Depth Prediction Model on NYU Depth v2

Input : Training data D_{train} from NYU Depth v2,
Learning rate η , Number of iterations T ,
Weights α, β, γ for loss terms

Output: Trained model θ

- 1 **Initialize the model and optimizer:**
- 2 $\theta \leftarrow$ Random Initialization ;
- 3 Optimizer \leftarrow Adam(θ, η);
- 4 $t \leftarrow 0$;
- 5 **while** $t < T$ **do**
- 6 **Load batch of training data:**
 $(x, y) \leftarrow$ LoadBatch(D_{train});
- 7 **Forward pass (IRv2 Encoder-Decoder):**
- 8 $z_{\text{encoder}} \leftarrow$ IRv2_Encoder(x);
- 9 $\hat{y} \leftarrow$ Decoder(z_{encoder});
- 10 **Compute total loss L_{total} :**
- 11 $L_{\text{depth}} \leftarrow$ MeanAbsoluteError(y, \hat{y});
- 12 $L_{\text{grad}} \leftarrow$ GradientEdgeLoss(y, \hat{y});
- 13 $L_{\text{SSIM}} \leftarrow$ SSIM_Loss(y, \hat{y});
- 14 $L_{\text{total}} \leftarrow \alpha L_{\text{depth}} + \beta L_{\text{grad}} + \gamma L_{\text{SSIM}}$;
- 15 **Backpropagation and update:**
- 16 Optimizer.zero_gradients();
- 17 L_{total} .backward();
- 18 Optimizer.step();
- 19 $t \leftarrow t + 1$;
- 20 **end**
- 21 **return** θ ;

4. Implementation

4.1. Dataset

We utilized the NYU Depth V2 dataset [10] to assess our suggested model. This contains RGB-D photos captured using the Microsoft Kinect sensor. It includes almost 1,400 densely annotated indoor scenes from 464 different locations, each one containing depth information and matching RGB photos. The dataset covers a variety of room types, such as living rooms, kitchens, and offices, as well as detailed per-pixel object tagging. From the 120,000 available samples in the dataset, a random subset of 65,000 samples was designated for training, while 654 samples were reserved for testing. We applied data augmentation to all images in the training set by horizontally flipping them while maintaining a constant height of 240 pixels to improve model training. The model generated predictions at a resolution of $240 \times 320 \times 3$, which is half the input size ($480 \times 640 \times 3$). For training, the input images are down-scaled to $240 \times 320 \times 3$, while the ground truth depth maps remain at their original resolution. Down-sampling reduces the computational load and speeds up training by decreasing the number of pixels the model needs to process, making it more efficient. During testing, the predicted depth map for the entire test image is computed and then up-scaled by a factor of two to match the ground truth resolution.

4.2. Environmental Setup

The proposed network was implemented using TensorFlow [33] environment. The model training was conducted

on an NVIDIA T4 GPU setup (2 GPUs), each with 16 GB of memory. The Adam [34] optimizer is used with AMSGrad enabled, a variant of gradient descent that adapts the learning rate dynamically was employed during training. Setting 0.0001 as the initial learning rate, and training was performed over 15 epochs. The default momentum parameters for Adam were maintained, with $\beta_1 = 0.9$ and $\beta_2 = 0.999$. The complete training process took approximately 5 hours with a batch size of 16. To mitigate overfitting, data augmentation techniques were applied, including horizontal flipping and cropping the height of the images to a constant size of 320 pixels. We did the same for other pre-trained models including VGG19 [35], ResNet50 [36], ResNet152 [36], DenseNet169 [37], and DenseNet201 [37]. These models varied in the number of parameters, and their performance was also varied with different error values and accuracy scores.

4.3. Evaluation Metrics

The error metrics used for evaluating the model's performance are defined by the following equations, which provide a quantitative assessment.

- Root Mean Squared Error (RMSE):

$$\text{RMSE} = \sqrt{\frac{1}{N} \sum_{i=1}^N (y_i - \hat{y}_i)^2} \quad (7)$$

- Log10 Error:

$$\text{Log10} = \frac{1}{N} \sum_{i=1}^N |\log_{10}(y_i) - \log_{10}(\hat{y}_i)| \quad (8)$$

- Absolute Relative Error (ARE):

$$\text{ARE} = \frac{1}{N} \sum_{i=1}^N \left| \frac{y_i - \hat{y}_i}{y_i} \right| \quad (9)$$

- Accuracy: Three different kinds of threshold values are used to evaluate the depth map's accuracy. A threshold in depth map prediction typically refers to a set of pre-defined limits within which the estimated depth values are considered to be accurate. The thresholds provide a straightforward way to evaluate the accuracy of depth predictions at different levels of precision.

$$\delta_i = \frac{1}{N} \sum_{i=1}^N \left(\max \left(\frac{y_i}{\hat{y}_i}, \frac{\hat{y}_i}{y_i} \right) < \text{th}_i \right), \quad (10)$$

where $\text{th}_i \in \{1.25, 1.25^2, 1.25^3\}$

where \hat{y}_i is a pixel in the expected depth image \hat{y} and y_i is a pixel in depth image y . The total number of pixels for each depth picture is N , and δ represents the accuracy corresponding to the respective threshold values.

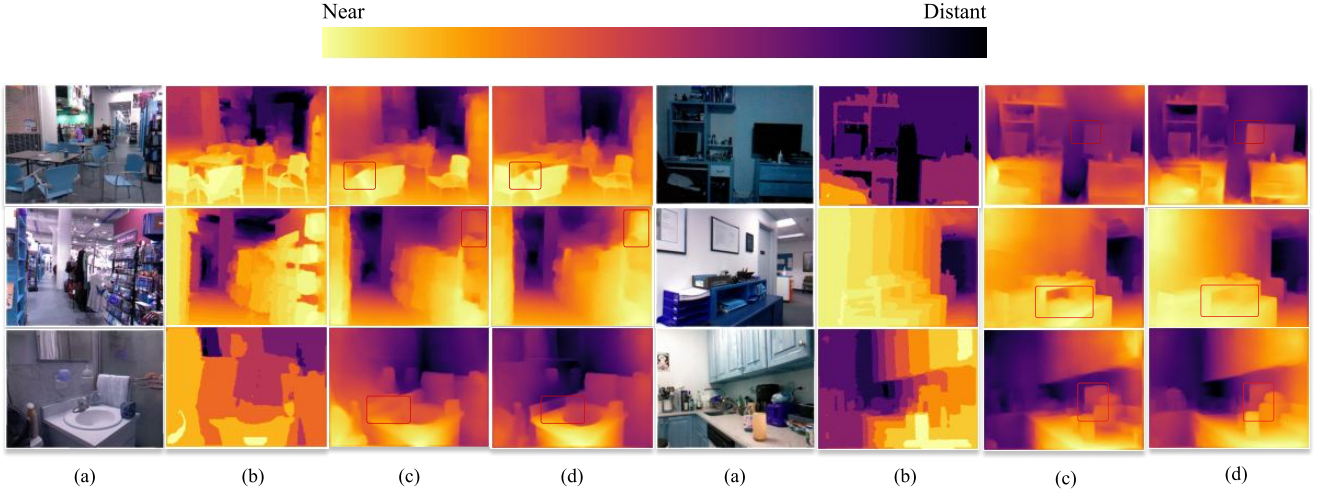


Figure 4: Monocular depth estimation on NYU-Depth v2 dataset using different encoder-decoder models: (c) Alhashim et al. [38] and (d) proposed. The input RGB image and ground truth depth map are shown by (a) and (b), respectively.

Table 2

Performance comparison of various encoder-decoder methods for depth estimation, where each method uses a different pre-trained encoder. All methods were implemented by the authors, with the proposed IRv2 model demonstrating superior performance across both error metrics and accuracy thresholds ($\delta < 1.25$, $\delta < 1.25^2$, $\delta < 1.25^3$).

Method	# of parameters	Error Metrics ↓			Accuracy ↑		
		ARE	RMSE	Log10	$\delta < 1.25$	$\delta < 1.25^2$	$\delta < 1.25^3$
Enc-Dec-DenseNet201	17.23M	0.101	0.320	0.051	0.831	0.956	0.979
Enc-Dec-ResNet152	15.54M	0.117	0.364	0.058	0.796	0.942	0.970
Enc-Dec-VGG19	22.37M	0.110	0.324	0.054	0.820	0.950	0.976
Enc-Dec-IRv2 (Proposed)	31.15M	0.064	0.228	0.032	0.893	0.967	0.985

5. Results

During training, the model's loss gradually decreases until it converges with the validation loss. At this stage, training is terminated, resulting in an optimal loss value (0.1523) for our model by selecting the appropriate number of epochs. Figure 5 illustrates the variations of training loss and validation loss after each epoch. From table 2, the proposed encoder-decoder method with IRv2 achieves a $\delta < 1.25$ accuracy of 0.893, which is significantly higher than most competing methods. This high accuracy at a strict threshold ($\delta < 1.25$) indicates that the method can reliably estimate depth with high precision, even when objects in the image are complex and vary in distance. In Figure 4, the outputs of two different models are presented. The marked areas for Alhashim et al. [38] (c) and our model (d) highlight the differences in depth prediction accuracy when compared to the ground truth depth map (b). From the marked area, it is evident that the complex objects or the complex portion of the objects are distinguished more precisely by our model. Besides, our model achieves the lowest ARE of 0.064, showing that it is more consistent in estimating depth values, with the lowest RMSE of 0.228, indicating that the predicted depth values align more closely with the true values. The model

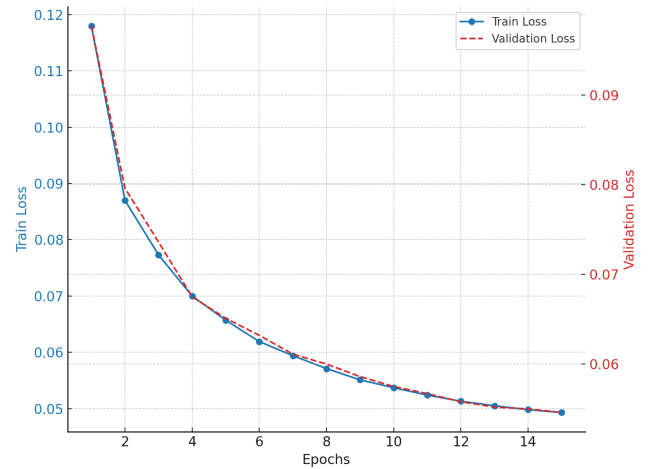


Figure 5: Train and Validation Loss over Epochs. This graph shows the decrease in both train loss (blue, solid line) and validation loss (red, dashed line) across 15 epochs.

also excels in the Log10 error, scoring 0.032, showing superior performance in minimizing the magnitude of error in the logarithmic scale.

The histograms located in the top-left and bottom-left corners of Figure 6 compare the R^2 scores of our proposed

Table 3

Performance comparison of various existing methods for depth estimation using error metrics and accuracy at different thresholds ($\delta < 1.25$, $\delta < 1.25^2$, $\delta < 1.25^3$), where the proposed model outperforms the others.

Method	Error Metrics ↓			Accuracy ↑		
	ARE	RMSE	Log10	$\delta < 1.25$	$\delta < 1.25^2$	$\delta < 1.25^3$
Rudolph et al. [39]	0.138	0.501	0.058	0.823	0.961	0.990
Basak et al. [40]	0.103	0.388	–	0.892	0.978	0.995
Alhashim et al. [38]	0.123	0.465	0.053	0.846	0.974	0.994
Lee et al. [26]	0.131	0.538	–	0.837	0.971	0.994
Xu et al. [27]	0.125	0.593	0.057	0.806	0.952	0.986
Jung et al. [15]	0.134	0.527	–	0.822	0.971	0.993
Li et al. (VGG16) [25]	0.152	0.611	0.064	0.789	0.955	0.988
Li et al. (VGG19) [25]	0.146	0.617	0.063	0.795	0.958	0.991
Li et al. (ResNet50) [25]	0.143	0.635	0.063	0.788	0.958	0.991
Enc-Dec-IRv2 (Proposed)	0.064	0.228	0.032	0.893	0.967	0.985

model (depicted in blue) against the encoder-decoder model using VGG19 and the architecture proposed by Alhashim et al. [38] (shown in orange). Additionally, the scatter plots on the right side of Figure 6 display the R^2 scores for individual test images. Our model significantly outperforms these alternatives, achieving an R^2 score of 0.8682.

6. Conclusion

This research presents a novel method for depth map production utilizing monocular depth estimation through an encoder-decoder architecture founded on the Inception-ResNet-v2 model. Our methodology employs multi-scale feature extraction and a composite loss function that integrates depth loss, gradient edge loss, and SSIM loss, resulting in a notable improvement in depth prediction accuracy, evidenced by an Absolute Relative Error (ARE) of 0.064, a Root Mean Square Error (RMSE) of 0.228, and a Log10 error of 0.032. These values demonstrate the model's precision in predicting accurate depth values. Furthermore, our model achieved 0.893 accuracy for $\delta < 1.25$, outperforming other approaches in complex scenarios with changing object sizes and distances. The findings demonstrate that our methodology is effective in generating precise depth maps, even in challenging environments. However, one noticeable drawback of our architecture is the comparatively large number of parameters. This can lead to increased computational requirements, making the model slower and more resource-intensive during training and inference. In real-time applications like autonomous driving or robotic navigation, this could cause latency, limiting the model's usefulness in resource-constrained environments like mobile devices.

Despite these limitations, improvements in error metrics combined with high accuracy make the model a promising model for real-world applications, offering more reliable depth predictions even in challenging and complex environments. The model's ability to generate accurate depth maps,

even in intricate and demanding situations, constitutes a significant advancement in the domain of monocular depth estimation. While the high processing demand may limit its employment in real-time applications, the significant improvements in accuracy justify the trade-off. In cases where precision is critical, such as autonomous systems and advanced image processing, our approach provides a robust and dependable response.

Declaration of Funding

This paper was not funded.

Author Contributions

All authors were involved in the conception and design, analysis and interpretation of the data, drafting of the manuscript and revising it critically for intellectual content, approving the final version for submission, and agreeing to be accountable for all aspects of the work.

Acknowledgements

This work is supported in part by the Khulna University of Engineering & Technology (KUET).

References

- [1] M. Carranza-García, F. Galan-Sales, J. M. Luna-Romera, J. Riquelme, Object detection using depth completion and camera-lidar fusion for autonomous driving, *Integrated Computer-Aided Engineering* 29 (2022) 1–18. doi:10.3233/ICA-220681.
- [2] W. Burger, M. J. Burge, Scale-invariant feature transform (sift), in: *Digital Image Processing: An Algorithmic Introduction*, Springer, 2022, pp. 709–763.
- [3] A. Quattoni, M. Collins, T. Darrell, Conditional random fields for object recognition, 2004.
- [4] Y. Kim, H. Jung, D. Min, K. Sohn, Deep monocular depth estimation via integration of global and local predictions, *IEEE Transactions on*

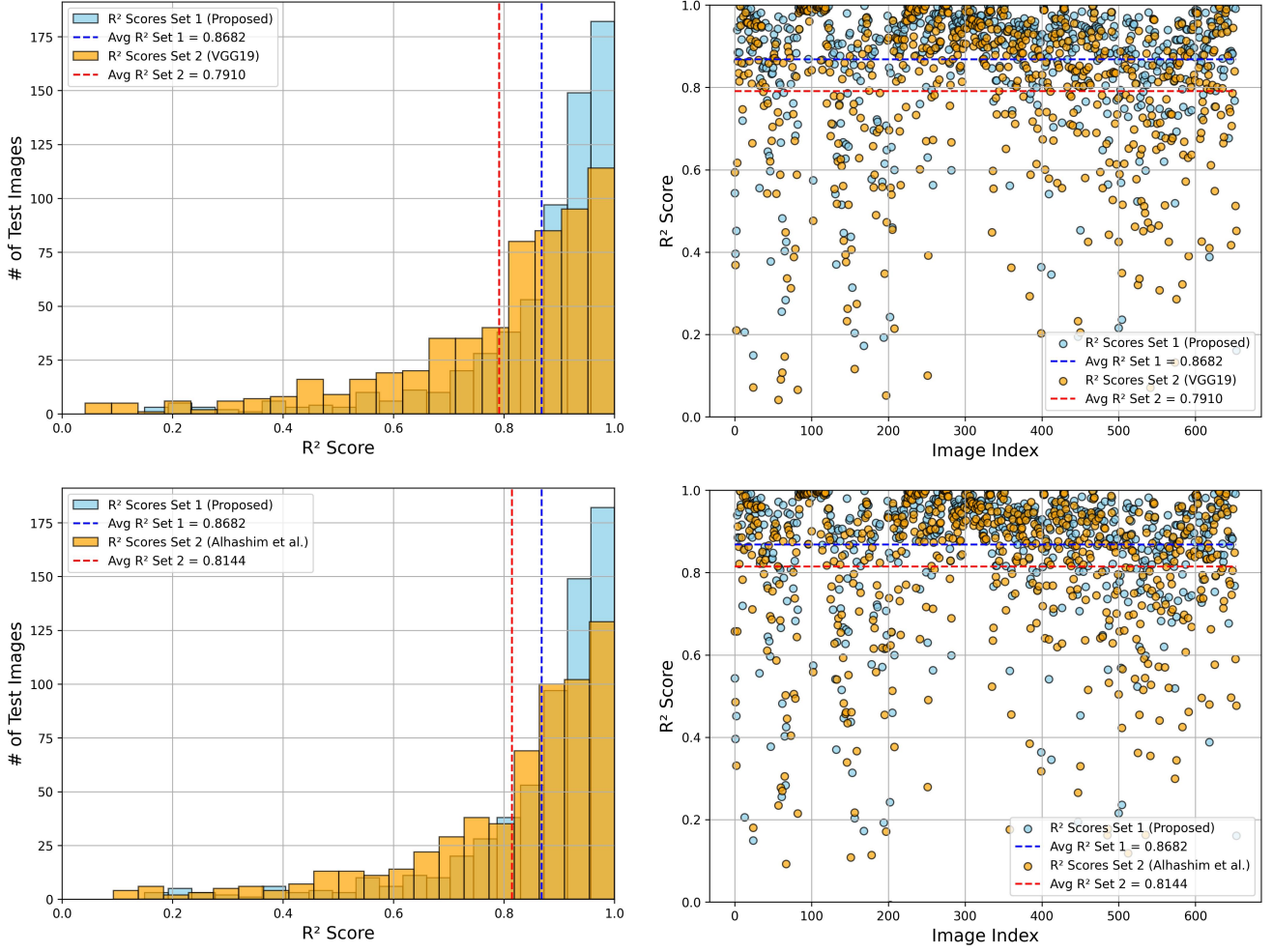


Figure 6: R² Scores for Monocular Depth Estimation Across Test Images for Two Models. The left plot shows the distribution of R² values (x-axis) with frequency (y-axis), while the right plot displays individual R² scores (y-axis) against image index (x-axis).

- Image Processing 27 (8) (2018) 4131–4144. doi:10.1109/TIP.2018.2836318.
- [5] I. Laina, C. Rupprecht, V. Belagiannis, F. Tombari, N. Navab, Deeper depth prediction with fully convolutional residual networks, in: 2016 Fourth International Conference on 3D Vision (3DV), 2016, pp. 239–248. doi:10.1109/3DV.2016.32.
 - [6] I. J. Goodfellow, J. Pouget-Abadie, M. Mirza, B. Xu, D. Warde-Farley, S. Ozair, A. Courville, Y. Bengio, Generative adversarial networks (2014). arXiv:1406.2661. URL <https://arxiv.org/abs/1406.2661>
 - [7] T. Schlett, C. Rathgeb, C. Busch, Deep learning-based single image face depth data enhancement, Computer Vision and Image Understanding 210 (2021) 103247. doi:https://doi.org/10.1016/j.cviu.2021.103247.
 - [8] X. Qiao, C. Ge, Y. Zhang, Y. Zhou, F. Tosi, M. Poggi, S. Mattoccia, Depth super-resolution from explicit and implicit high-frequency features, Computer Vision and Image Understanding 237 (2023) 103841. doi:https://doi.org/10.1016/j.cviu.2023.103841.
 - [9] C. Szegedy, S. Ioffe, V. Vanhoucke, A. Alemi, Inception-v4, inception-resnet and the impact of residual connections on learning (2016). arXiv:1602.07261. URL <https://arxiv.org/abs/1602.07261>
 - [10] N. Silberman, D. Hoiem, P. Kohli, R. Fergus, Indoor segmentation and support inference from rgb-d images, in: Computer Vision, ECCV 2012 - 12th European Conference on Computer Vision, Proceedings, part 5 Edition, no. PART 5 in Lecture Notes in Computer Science (including subseries Lecture Notes in Artificial Intelligence and Lecture Notes in Bioinformatics), 2012, pp. 746–760, 12th European Conference on Computer Vision, ECCV 2012 ; Conference date: 07-10-2012 Through 13-10-2012. doi:10.1007/978-3-642-33715-4_54.
 - [11] A. C. Kumar, S. M. Bhandarkar, M. Prasad, Depthnet: A recurrent neural network architecture for monocular depth prediction, in: 2018 IEEE/CVF Conference on Computer Vision and Pattern Recognition Workshops (CVPRW), 2018, pp. 396–3968. doi:10.1109/CVPRW.2018.00066.
 - [12] X. SHI, Z. Chen, H. Wang, D.-Y. Yeung, W.-k. Wong, W.-c. WOO, Convolutional lstm network: A machine learning approach for precipitation nowcasting, in: C. Cortes, N. Lawrence, D. Lee, M. Sugiyama, R. Garnett (Eds.), Advances in Neural Information Processing Systems, Vol. 28, Curran Associates, Inc., 2015. URL https://proceedings.neurips.cc/paper_files/paper/2015/file/07563a3fe3bbe7e3ba84431ad9d055af-Paper.pdf
 - [13] A. Geiger, P. Lenz, C. Stiller, R. Urtasun, Vision meets robotics: the kitti dataset, The International Journal of Robotics Research 32 (2013) 1231–1237. doi:10.1177/0278364913491297.
 - [14] M. Mancini, G. Costante, P. Valigi, T. A. Ciarfuglia, J. Delmerico, D. Scaramuzza, Toward domain independence for learning-based monocular depth estimation, IEEE Robotics and Automation Letters 2 (3) (2017) 1778–1785.
 - [15] H. Jung, Y. Kim, D. Min, C. Oh, K. Sohn, Depth prediction from a

- single image with conditional adversarial networks, 2017, pp. 1717–1721. doi:10.1109/ICIP.2017.8296575.
- [16] K. G. Lore, K. Reddy, M. Giering, E. A. Bernal, Generative adversarial networks for depth map estimation from rgb video, in: 2018 IEEE/CVF Conference on Computer Vision and Pattern Recognition Workshops (CVPRW), 2018, pp. 1258–12588. doi:10.1109/CVPRW.2018.00163.
 - [17] T. Feng, D. Gu, Sganvo: Unsupervised deep visual odometry and depth estimation with stacked generative adversarial networks, IEEE Robotics and Automation Letters 4 (4) (2019) 4431–4437. doi:10.1109/Lra.2019.2925555. URL <http://dx.doi.org/10.1109/LRA.2019.2925555>
 - [18] F. Aleotti, F. Tosi, M. Poggi, S. Mattoccia, Generative Adversarial Networks for Unsupervised Monocular Depth Prediction: Munich, Germany, September 8–14, 2018, Proceedings, Part I, 2019, pp. 337–354. doi:10.1007/978-3-030-11009-3_20.
 - [19] M. Cordts, M. Omran, S. Ramos, T. Rehfeld, M. Enzweiler, R. Benenson, U. Franke, S. Roth, B. Schiele, The cityscapes dataset for semantic urban scene understanding (2016). arXiv:1604.01685. URL <https://arxiv.org/abs/1604.01685>
 - [20] Y. Li, K. Qian, T. Huang, J. Zhou, Depth estimation from monocular image and coarse depth points based on conditional gan, MATEC Web of Conferences 175 (2018) 03055. doi:10.1051/mateconf/201817503055.
 - [21] Y. Almaloglu, M. R. U. Saputra, P. P. B. d. Gusmão, A. Markham, N. Trigoni, Ganvo: Unsupervised deep monocular visual odometry and depth estimation with generative adversarial networks, in: 2019 International Conference on Robotics and Automation (ICRA), 2019, pp. 5474–5480. doi:10.1109/ICRA.2019.8793512.
 - [22] A. Resindra, Y. Monno, M. Okutomi, S. Suzuki, T. Gotoda, K. Miki, Self-supervised monocular depth estimation in gastroendoscopy using gan-augmented images, 2021, p. 35. doi:10.1117/12.2579317.
 - [23] A. Rau, P. Edwards, O. Ahmad, P. Riordan, M. Janatka, L. Lovat, D. Stoyanov, Implicit domain adaptation with conditional generative adversarial networks for depth prediction in endoscopy, International Journal of Computer Assisted Radiology and Surgery 14 (04 2019). doi:10.1007/s11548-019-01962-w.
 - [24] W. Kim, C.-H. Jeong, S. Kim, Improvements in deep learning-based precipitation nowcasting using major atmospheric factors with radar rain rate, Computers & Geosciences 184 (2024) 105529. doi:https://doi.org/10.1016/j.cageo.2024.105529. URL <https://www.sciencedirect.com/science/article/pii/S0098300424000128>
 - [25] J. Li, R. Klein, A. Yao, A two-streamed network for estimating fine-scaled depth maps from single rgb images (2017). arXiv:1607.00730. URL <https://arxiv.org/abs/1607.00730>
 - [26] J. Lee, C.-S. Kim, Monocular depth estimation using relative depth maps, 2019. doi:10.1109/CVPR.2019.00996.
 - [27] D. Xu, W. Wang, H. Tang, H. Liu, N. Sebe, E. Ricci, Structured attention guided convolutional neural fields for monocular depth estimation (2018). arXiv:1803.11029. URL <https://arxiv.org/abs/1803.11029>
 - [28] D. Zoran, P. Isola, D. Krishnan, W. T. Freeman, Learning ordinal relationships for mid-level vision, in: Proceedings of the IEEE International Conference on Computer Vision (ICCV), 2015.
 - [29] K. Simonyan, A. Zisserman, Very deep convolutional networks for large-scale image recognition (2015). arXiv:1409.1556. URL <https://arxiv.org/abs/1409.1556>
 - [30] W. Chen, Z. Fu, D. Yang, J. Deng, Single-image depth perception in the wild (2017). arXiv:1604.03901. URL <https://arxiv.org/abs/1604.03901>
 - [31] Z. Zhang, C. Xu, J. Yang, J. Gao, Z. Cui, Progressive hard-mining network for monocular depth estimation, IEEE Transactions on Image Processing 27 (8) (2018) 3691–3702. doi:10.1109/TIP.2018.2821979.
 - [32] A. Saxena, M. Sun, A. Ng, Make3d: Learning 3d scene structure from a single still image, IEEE transactions on pattern analysis and machine intelligence 31 (2009) 824–40. doi:10.1109/TPAMI.2008.132.
 - [33] M. Abadi, P. Barham, J. Chen, Z. Chen, A. Davis, J. Dean, M. Devin, S. Ghemawat, G. Irving, M. Isard, M. Kudlur, J. Levenberg, R. Monga, S. Moore, D. G. Murray, B. Steiner, P. Tucker, V. Vasudevan, P. Warden, M. Wicke, Y. Yu, X. Zheng, Tensorflow: A system for large-scale machine learning (2016). arXiv:1605.08695. URL <https://arxiv.org/abs/1605.08695>
 - [34] S. J. Reddi, S. Kale, S. Kumar, On the convergence of adam and beyond (2019). arXiv:1904.09237. URL <https://arxiv.org/abs/1904.09237>
 - [35] V. Sudha, D. Ganeshbabu, A convolutional neural network classifier vgg-19 architecture for lesion detection and grading in diabetic retinopathy based on deep learning, Computers, Materials & Continua 66 (2020) 827–842. doi:10.32604/cmc.2020.012008.
 - [36] K. He, X. Zhang, S. Ren, J. Sun, Deep residual learning for image recognition (2015). arXiv:1512.03385. URL <https://arxiv.org/abs/1512.03385>
 - [37] G. Huang, Z. Liu, L. van der Maaten, K. Q. Weinberger, Densely connected convolutional networks (2018). arXiv:1608.06993. URL <https://arxiv.org/abs/1608.06993>
 - [38] I. Alhashim, P. Wonka, High quality monocular depth estimation via transfer learning (2019). arXiv:1812.11941. URL <https://arxiv.org/abs/1812.11941>
 - [39] M. Rudolph, Y. Dawoud, R. Gildenring, L. Nalpantidis, V. Belagianis, Lightweight monocular depth estimation through guided decoding (2022). arXiv:2203.04206. URL <https://arxiv.org/abs/2203.04206>
 - [40] H. Basak, S. Ghosal, M. Sarkar, M. Das, S. Chattopadhyay, Monocular depth estimation using encoder-decoder architecture and transfer learning from single rgb image, 2020, pp. 1–6. doi:10.1109/UPCON50219.2020.9376365.